ACS central science

Research Article

Cite This: ACS Cent. Sci. 2018, 4, 277−287

Dealloyed Intra-Nanogap Particles with Highly Robust, Quantifiable Surface-Enhanced Raman Scattering Signals for Biosensing and Bioimaging Applications

Minho Kim, Sung Min Ko, Jae-Myoung Kim, Jiwoong Son, Chungyeon Lee, Won-Kyu Rhim, and Jwa-Min Nam*

Department of Chemistry, Seoul National University, Seoul 08826, South Korea

Supporting Information

ABSTRACT: Uniformly controlling a large number of metal nanostructures with a plasmonically enhanced signal to generate quantitative optical signals and the widespread use of these structures for surface-enhanced Raman scattering (SERS)-based biosensing and bioimaging applications are of paramount importance but are extremely challenging. Here, we report a highly controllable, facile selective-interdiffusive dealloying chemistry for synthesizing the dealloyed intra-nanogap particles (DIPs) with a ∼2 nm intragap in a high yield (∼95%) without the need for an interlayer. The SERS signals from DIPs are highly quantitative and polarization-independent with polarized laser sources. Remarkably, all the analyzed particles displayed the SERS enhancement factors (EFs) of $\geq 1.1 \times 10^8$ with a very narrow distribution of EFs. Finally, we show that DIPs can be used as ultrasensitive SERS-based DNA detection probes for detecting 10 aM to 1 pM target concentrations and highly robust, quantitative real-time cell imaging probes for long-term imaging with low laser power and short exposure time.

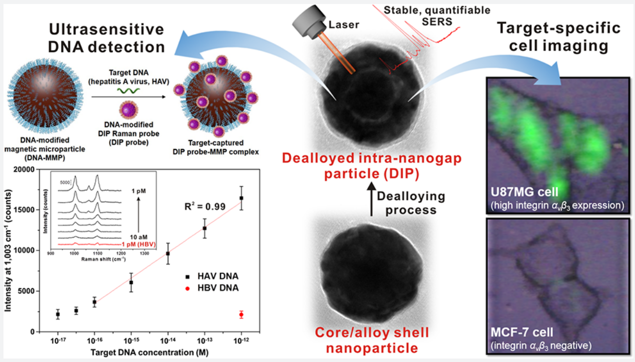

INTRODUCTION

Plasmonic nanostructures, particularly with a plasmonically coupled and enhanced nanogap, are of paramount importance and interest due to their strong, tunable optical properties and enormous potential in various applications including catalysis, sensing, and imaging.[1−4] Because the optical properties of plasmonic nanostructures are highly dependent on various nanostructural features, highly precise synthesis of plasmonic nanostructures in a high yield is needed to obtain controllable, quantifiable plasmonic signals from these nanostructures. Among many plasmonically enhanced optical signals, surface−enhanced Raman scattering (SERS) has received lots of attention because of its ultrahigh sensitivity, which can be extended to single-molecule-level sensitivity and multiplexing potential.[5] In this regard, SERS-based techniques are being exploited widely in plasmonics and analytical applications, including for biosensing and the detection of chemical warfare agents.[6,7] In plasmonics, it is now well-known that the excitation of localized surface plasmon resonances in nanoparticles (NPs) of noble metals (in particular, those of Au and Ag) can significantly enhance and localize the electromagnetic (EM) field at specific locations between NPs, which are called "hot spots".[8−10] There have been numerous attempts to design and produce SERS-active structures by using morphology-controlled noble metal nanostructures, such as nanotips, nanopores, and nanoscale-roughened surfaces.[11−13] In particular, with respect to SERS, the EM field can also be enhanced significantly via plasmonic coupling at the gaps or junctions between metallic nanostructures.[14] However, the plasmonic coupling in these gaps is largely affected by the interparticle distance, which, in turn, has a marked effect on the SERS signal.[15] This can induce uncontrollable irreproducibility in the SERS signal, which is a major barrier for these SERS-active structures to be useful for practical applications. Consequently, a high-precision nanometer scale or sub-nanometer scale gap engineering for a large number of these nanostructures is a key challenge for generating reproducible and reliable SERS signals from these particles.[1,16,17]

Among many plasmonic nanogap structures,[1] intra-nanogap structures with a nanometer-scale interior gap are highly promising as SERS substrates because of their uniformity and controllability in nanogaps over a large number of particles, resulting in strongly enhanced and tunable SERS signals. To form SERS-active interior nanogap structures, various synthetic strategies have been adopted.[18−20] In particular, it was shown that thiolated DNA on AuNPs can facilitate the formation of a 1 nm interior gap during the Au−Au core−shell formation process and generate Au nanobridged nanogap particles (Au-NNPs) with a uniform 1 nm intragap in a high yield and strong,

Received: December 6, 2017
Published: January 17, 2018

DOI: 10.1021/acscentsci.7b00584

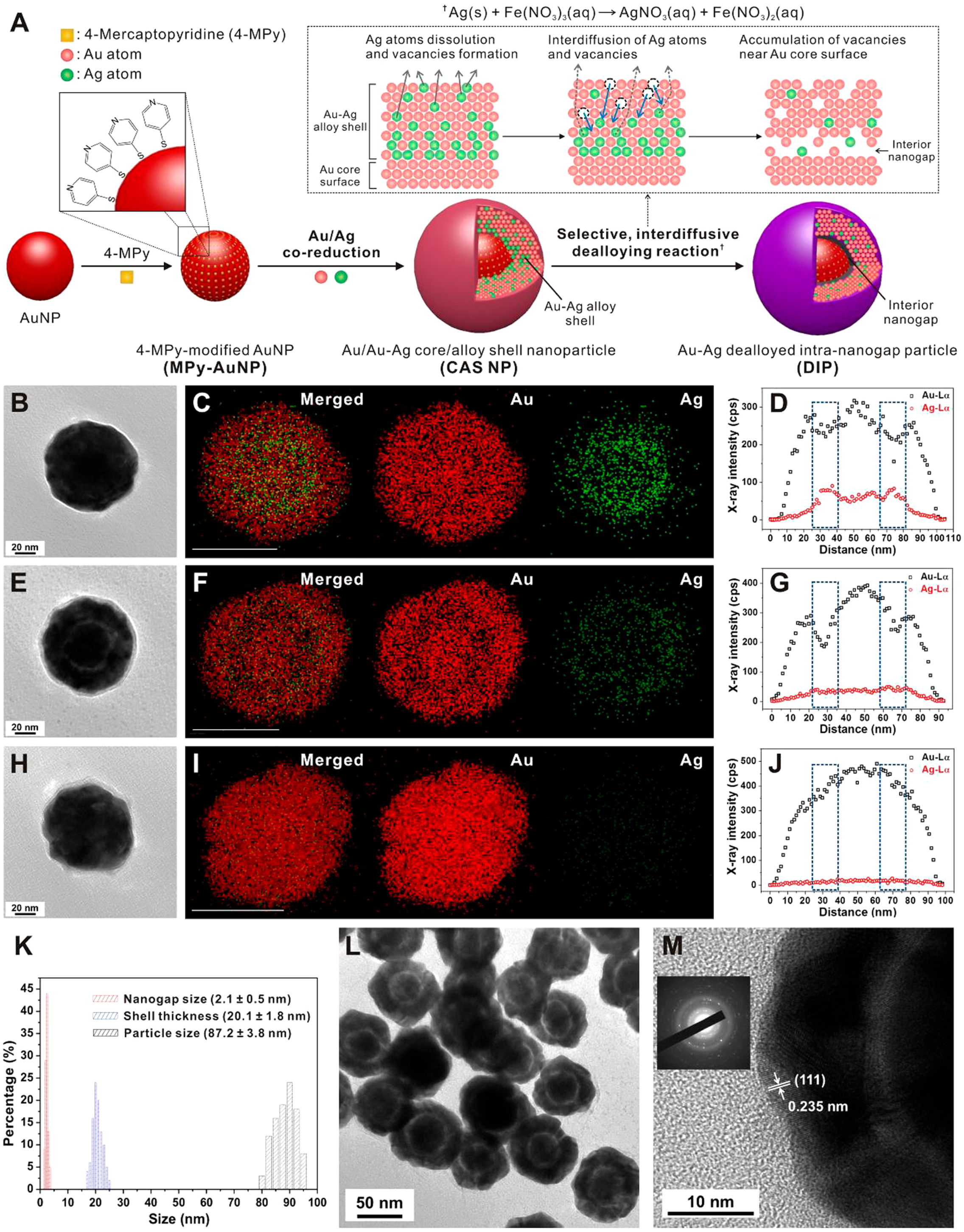

Figure 1. Synthetic strategy and characterization of dealloyed internanogap particles. (A) Schematic illustration of the selective, interdiffusive dealloying (SID)-based strategy for the synthesis of the Au−Ag dealloyed intra-nanogap particles (DIPs) from Au/Au−Ag core/alloy shell (CAS) NPs. The proposed mechanism of the SID reaction is shown in the black dotted box. (B−J) TEM images, EDX elemental mapping and EDX line scan profiles across the centers of NPs: (B−D) CAS NPs, (E−G) DIPs, and (H−J) gap-less Au−Au core−shell NPs. Ag atoms are primarily located near the Au core in a CAS NP (the blue dotted boxes in panel D) and the number of Ag atoms near the Au core decreases after the dealloying reaction (the blue dotted boxes in panel G), resulting in the interior nanogap. For gap-less AuNPs, an interior nanogap was not observed (the blue dotted boxes in panel J). The EDX map of Ag in panel I shows noise-level signals. The white scale bars are 50 nm. (K) Nanogap size, shell thickness, and particle size distributions of DIPs (the HR-TEM images of 100 particles were analyzed). (L) TEM image of DIPs. (M) HR-TEM image of a DIP. Here, *d*-spacing of 0.235 nm for adjacent lattice fringes corresponds to (111) planes of a face-centered cubic structure. The inset shows a ring-shaped SAED pattern of a DIP, indicating there is a polycrystalline structure.

stable, and reproducible SERS signals.[21,22] Other approaches in generating interior nanogap structures such as silica(SiO_2)-interlayered nanogap structures with Au core and Au shell (Au nanomatryoshka) and polymer or small molecule-interlayered plasmonic nanogap structures have been adopted to synthesize various intra-nanogap structures.[18−20] All these structures,

DOI: 10.1021/acscentsci.7b00584
ACS Cent. Sci. 2018, 4, 277−287

however, still need to address many drawbacks and challenges such as complicated synthetic complexity, time and cost, reaction conditions including temperature, nanometer-level structural precision, limitation in large-scale production, particle stability, versatility in structure and composition, and lack of practical applications. It should be noted that the need for an interlayer to form intra-nanogaps inside particles and laser polarization-dependent changes in optical signals from intra-nanogap particles largely limit understanding and controlling the plasmonic properties of these nanostructures including electromagnetic field intensity and distribution. Importantly, the use and advantageous properties of these intra-nanogap particles for biomedical applications have not been well explored nor clearly shown.

Here, we present a straightforward, facile and generally applicable synthetic strategy for forming dealloyed intra-nanogap particles (DIPs) with an interlayer-free intra-nanogap in a high yield via the selective-interdiffusive dealloying (SID) process at room temperature, and it is shown that these DIPs can generate strong, quantifiable laser polarization-independent SERS signals (Figure 1A). Importantly, biologically functionalized DIPs can be used for detecting DNA in a highly sensitive and quantitative manner and also for targeting and imaging cancer cells for highly reliable, quantitative, and long-term subcellular bioimaging applications. As the highly controllable dealloying reaction progresses with the DIPs, a nanometer-sized interior gap was formed on Au core surface via selective Ag-etching and interdiffusion of Ag atoms (SID process), resulting in the formation of NPs with a ~2 nm interior gap in high yield (~95%). It should be noted that this SID process can spontaneously happen at room temperature due to the nature of the corrosion process occurring in the presence of etchants or oxidants even at the low temperature. Remarkably, the interior nanogap was uniformly formed with randomly distributed metal residues in a symmetric fashion, leading the polarization-independent SERS signals from the Raman dyes in the interior gaps of these structures, and the SERS signal intensity linearly increases as the particle concentration increases, allowing for highly reliable, quantitative SERS. Remarkably, all the particles (110 particles) displayed SERS enhancement factors of $\geq 1.1 \times 10^8$ with a very narrow distribution of EFs. Importantly, Au-gap-Au/Ag DIPs were modified with DNA for DNA sensing applications, and the assay results show that these DNA-modified DIPs generate highly quantitative and sensitive DNA detection results, ranging from aM to pM target concentrations. Finally, these DIPs were functionalized with cell-targeting peptides for cell imaging applications. The results suggest that the peptide-modified DIPs can selectively target integrin $\alpha_v\beta_3$ expression cells and allow for *in situ* long-term (>30 min) real-time SERS imaging intracellular regions with low laser power and short exposure time in a highly reliable, quantifiable manner.

■ RESULTS AND DISCUSSION

Selective, Interdiffusive Dealloying-Based Synthesis of Nanoparticles with an Interlayer-Free Interior Nanogap. To synthesize the DIPs with the SID process, we first formed Au/Au–Ag core/alloy shell nanoparticles (CAS NPs) through a coreduction process involving the simultaneous reduction of $HAuCl_4$ and $AgNO_3$ on 4-MPy-modified AuNPs (MPy-AuNPs) (Figure 1B). The average size of CAS NPs, as measured from transmission electron microscopy (TEM) images, was ~87.0 nm (Figure S1), while the atomic composition of the shell region was estimated to be $Au_{77.2}Ag_{22.8}$ (Table S1). Interestingly, the reduced Au and Ag atoms were not evenly distributed throughout the entire shell region (Figure 1C and Figure S2A). An energy-dispersive X-ray spectroscopy (EDX) line scan performed across the centers of the CAS NPs showed that most of the Ag atoms were located near the Au core, with the number of Au atoms decreasing near the Au core (Figure 1D, the blue dotted box). In general, a higher standard reduction potential of the Au precursor results in faster reduction as compared to the case for the Ag precursor ($AuCl_4^-/Au$ = 0.99 V and Ag^+/Ag = 0.8 V versus standard hydrogen electrode).[23] The strong affinity between Ag and the pyrrolidone groups of polyvinylpyrrolidone (PVP) help increase the reduction rate of the Ag precursor in the early stage,[24,25] which results in the accumulation of Ag atoms at a faster rate near the Au core. This result is in good agreement with previously reported results.[26] To examine this phenomenon in more detail, we monitored the changes in the extinction peak of the CAS NPs during the alloy shell formation process (Figure S3). In the early stage of the formation process, the extinction peak exhibited a rapid blue shift, suggesting the formation of Ag layers. As the reaction progressed, the extinction peak underwent a gradual red shift, with the intensity of the peak increasing; this was indicative of the formation of larger CAS NPs.

Next, we introduced ferric nitrate $[Fe(NO_3)_3]$ into the CAS NPs to selectively dissolve the Ag atoms (Figure 1A). It can be seen from Figure 1E that the Ag-etched CAS NPs have a nanogap present between the core and the shell via the dealloying process. The average size of the DIPs (~87.2 nm) was similar to that of the CAS NPs, with the interior nanogap and the shell size of the DIPs being ~2.1 and 20.1 nm, respectively (Figure 1K). The EDX elemental maps of the DIPs confirm that the Ag atoms near the Au core were almost completely etched away (Figure 1F and Figure S2B), and the EDX line scan profile indicates that the number of Ag atoms near the Au core dramatically decreased after the dealloying reaction (Figure 1G, blue dotted box); the proportion of Ag atoms in the shell region was lower as compared to that in the CAS NPs (Table S1). Furthermore, the Au-Lα curve for the area near the Au core was valley-shaped, when the Ag-Lα peak disappeared (Figure 1G, blue dotted box), confirming that the interior nanogap is formed by the highly selective removal of Ag atoms near the Au core. In contrast to the case for the DIPs, an interior nanogap was not observed in the case of the gap-less Au/Au core/shell NPs (gap-less AuNPs), whose shell was composed only of Au and not a Au–Ag alloy (Figure 1H). The average size of the gap-less AuNPs was also similar to that of the CAS NPs (Figure S1), with the shell being composed entirely of Au atoms (Figure 1I, Figure S2C and Table S1). Further, a valley-like Au-Lα plot was not observed (Figure 1J, blue dotted box), confirming that the NPs had a nanogap-less structure. When $Fe(NO_3)_3$ was introduced into the as-synthesized gap-less AuNPs, there was no change in the morphology or the ultraviolet–visible (UV–vis) and SERS spectra of the NPs, suggesting that the ferric nitrate-based dealloying reaction only dissolves Ag (Figure S4). This synthesis strategy led to the fabrication of DIPs in a yield of ~95% (Figure 1L). The *d*-spacing of the adjacent lattice fringes of the DIPs was 0.235 nm, and their selected-area electron diffraction (SAED) was ring-like; the former corresponded to the (111) planes of a face-centered cubic structure while the latter was indicative of polycrystallinity (Figure 1M).

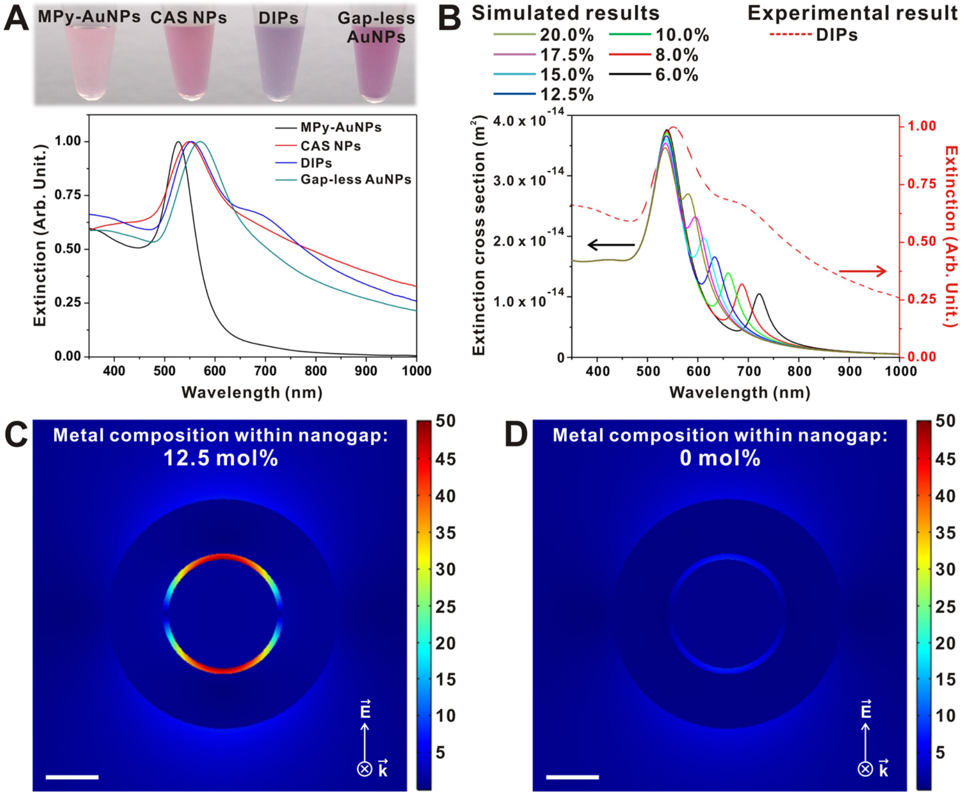

Figure 2. Experimental UV−vis spectra of NPs and theoretical calculation of DIPs. (A) UV−vis spectra of as-synthesized NPs. Inset: colors of NP solutions. (B) Simulated extinction spectra of DIPs with varying metal compositions within the interior nanogap. The interior-nanogap region is filled with a mixture of metal residues and water in this model. (C and D) Calculated electric near-field EM field distributions of the DIPs containing different compositions of metal residues within the interior nanogap [(C) 12.5 mol % and (D) 0 mol %]. The excitation wavelength is 633 nm. Scale bar is 20 nm.

To investigate the evolution of the interior nanogap, we monitored the structural changes as the CAS NPs transformed into DIPs through the dealloying reaction while increasing the amount of $Fe(NO_3)_3$ added (Figure S5). The mechanism proposed to explain the formation of the interior-nanogap structure is shown below (Figure 1A, see the proposed mechanism in the black dotted box). Once the $Fe(NO_3)_3$ solution is injected into the CAS NPs, the Ag atoms near the shell surface start getting dissolved by the $Fe(NO_3)_3$ (the gray line in a schematic of the proposed mechanism), and $Fe(NO_3)_3$ penetrates the CAS NPs through the Ag-etched sites. As the dealloying reaction progresses, pinhole-like vacancies (the black dotted open circles in the proposed mechanism) generated at the Ag-etched sites diffuse inward (the blue lines in the proposed mechanism), while metal atoms (mainly Ag atoms) diffuse outward because of the nanometer-scale Kirkendall effect.[27] Because the diffusion of Ag in Au is faster than that of Au in Ag in the case of the Au−Au alloy system, the net flux of the metals (Au and Ag) is mainly dependent on the diffusion rate of Ag; this results in a net flux of vacancies from the shell surface to the Au core.[27] Thus, the diffused Ag atoms are continually removed by the $Fe(NO_3)_3$ (the gray dotted lines in the proposed mechanism). Meanwhile, Au atoms diffuse to a smaller degree and interconnect with each other to minimize their surface energy. As this reaction continues, the accumulated vacancies near the Au core eventually result in the formation of a nanogap, while the interconnected Au atoms form a dense shell. In similarity to the proposed mechanism, the Ag atoms were partially etched and formed an incomplete interior nanogap when a small amount of $Fe(NO_3)_3$ (5 mM) was used. However, the number of dissolved Ag atoms was higher (10 mM), and an interior nanogap was uniformly formed when a large amount of $Fe(NO_3)_3$ was used (>15 mM) (Figure S5).

Owing to the morphological differences between the structures with (DIPs) and without (CAS NPs and gap-less AuNPs) a nanogap, the UV−vis spectra of these structures were also different (Figure 2A). Further, with formation of the shell structure, the color of the particle solution changed from pink (MPy-AuNPs) to dark pink (CAS NPs), then to blue-violet (DIPs), and finally to red-violet (gap-less AuNPs), as shown in Figure 2A. Furthermore, the extinction peaks of the NPs with the shell structure were red-shifted compared to those of the shell-less NPs (λ = 528, 549, 554, and 571 nm for the MPy-AuNPs, CAS NPs, DIPs, and gap-less AuNPs, respectively); however, a new extinction shoulder peak was observed at ∼700 nm in the case of NPs with the interior nanogap (DIPs). To elucidate the origin of this plasmonic peak from DIPs and study the optical properties of the nanogap region, we performed a computational simulation based on the Mie theory.[28] In our model, metal residues exist and are randomly distributed in the intra-nanogap region, and partially interconnect the core and the shell. The intra-nanogap region was modeled as a mixture of metal residues and water, and the effective dielectric function of the gap region was calculated using the Smith's approach that describes metallic behavior of mixtures with low metallic volume fraction (see details in Supporting Information).[29] A new extinction peak appears at a

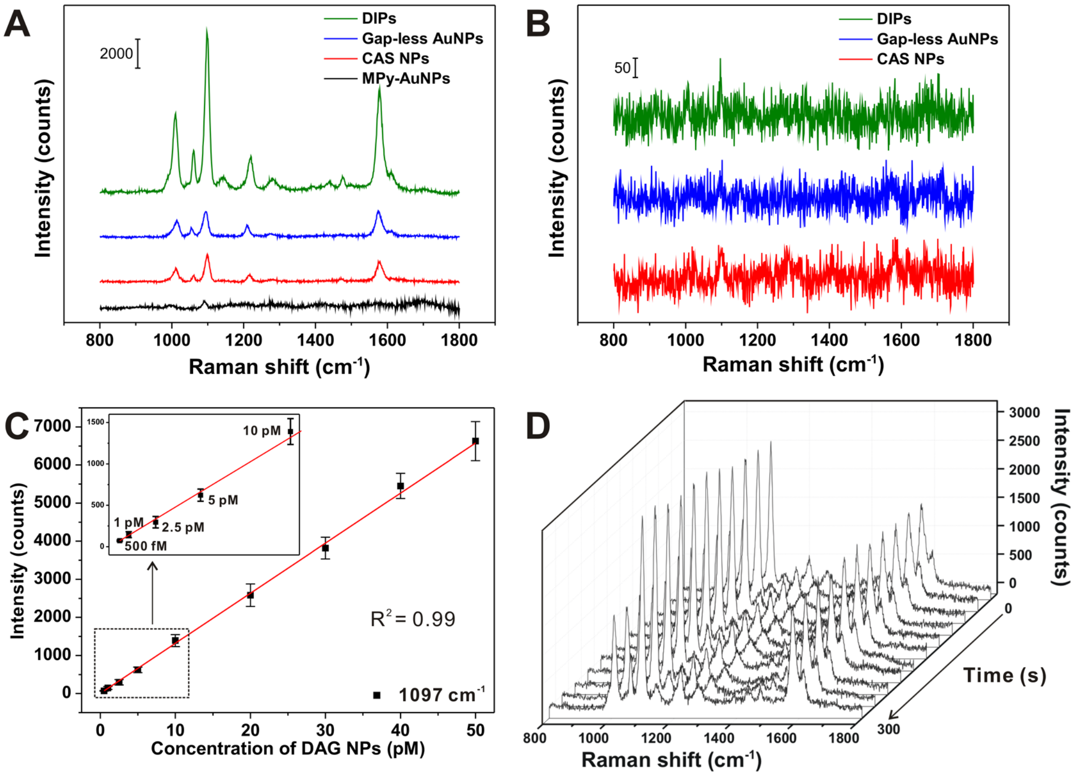

Figure 3. Nanostructure, Raman-dye position, particle concentration, and time-dependent SERS properties of as-synthesized NPs in solution. (A) SERS spectra of as-synthesized NPs in solution. Raman-dye molecules (4-MPy) were attached to Au core surfaces. (B) Solution-based SERS spectra of 4-MPy-modified NPs (all the dyes were modified to particle surfaces). (C) Particle concentration-dependent changes in SERS signal intensity with DIPs (500 fM to 50 pM; 1097 cm^{-1}). (D) Time-dependent Raman profiles of DIPs. All the spectra were acquired using 633 nm excitation laser at laser power of 4 mW and acquisition time of 10 s. Particle concentration was (A and B) 100 pM and (D) 20 pM.

longer wavelength (~950 nm) when an interior nanogap, filled with water, is formed inside an NP (Figure S6).[20] When the intra-nanogap region is filled with a mixture of metal residues and water, however, the resonance peak was blue-shifted from a longer wavelength region by changing the optical/physical state (e.g., effective dielectric function) of the nanogap. In addition, the resonance peak was continuously red-shifted as metal composition in the nanogap decreased (Figure 2B). This trend is well matched with changes in the UV−vis spectra of DIPs for different degrees of the dealloying reaction (Figure S5). Since the degree of etching for each DIP in solution should be slightly different, the broadened shoulder peak from the experimental result can be explained by the superposition of UV−vis spectra of DIPs with different metal compositions in the nanogap. Figure 2C shows the calculated near-field EM field distribution of the DIP containing 12.5 mol % of metal residues within the nanogap. Unlike the DIPs with a water-filled intra-nanogap (Figure 2D), the DIPs with a metal residue-filled nanogap generated a highly enhanced EM field, indicating that the metal residues within the interior nanogap play an important role in EM field enhancement.

SERS Analysis of DIPs in Solution. Next, we compared the solution-state SERS signals obtained from the as-synthesized NPs with respect to the fingerprint peak at 1097 cm^{-1} (Figure 3A). As compared to the SERS signal intensity of the shell-less Au NPs (MPy-AuNPs), those of the CAS NPs, gap-less AuNPs, and DIPs, were ~8.6, 7.7, and 50 times higher, respectively. In this case, Raman reporter molecules (4-MPy) were positioned in the interior-nanogap region. Both types of nanogap-less NPs (CAS NPs and gap-less AuNPs) showed similar increases in the SERS intensity. Thus, it can be concluded that it is the interior nanogap that ensures a highly enhanced SERS signal and that the composition of the metallic phase has only a minor effect on the SERS phenomenon. To examine the role of interior nanogap on SERS enhancement further, we placed the Raman reporter molecules (4-MPy) on the outmost shell surface instead of the Au core surface (Figure 3B). Irrespective of whether an interior nanogap was present or not, all similar-sized NPs (CAS NPs, gap-less AuNPs, and DIPs) showed a similar SERS signal, which was very weak. This result clearly suggests that the markedly stronger SERS enhancement was primarily attributable to the greater enhancement of the EM field in the interior nanogap.

Owing to the highly enhanced EM field and the uniformly confined hot spots in the interior nanogap, the SERS signal of the solution of the DIPs could be detected even at a very low concentration (500 fM), with there being a highly linear relationship ($R^2 = 0.99$) between the NP concentration and the SERS signal intensity (Figure 3C). In addition, we obtained stable SERS signals during time-course measurements performed under continuous laser exposure (Figure 3D). These experimental results indicate that the DIPs generated highly robust and sustainable SERS signals because of the Raman molecules stably encapsulated within highly SERS-active narrow interior nanogap. This property of the DIPs, wherein they produce uniform and quantitatively reproducible SERS signals with high sensitivity, can be exploited for biosensing/imaging. In addition, the DIPs were highly responsive under excitation at a wavelength of 785 nm (Figure S7); this suggests that they should be suitable for use for *in*/*ex*

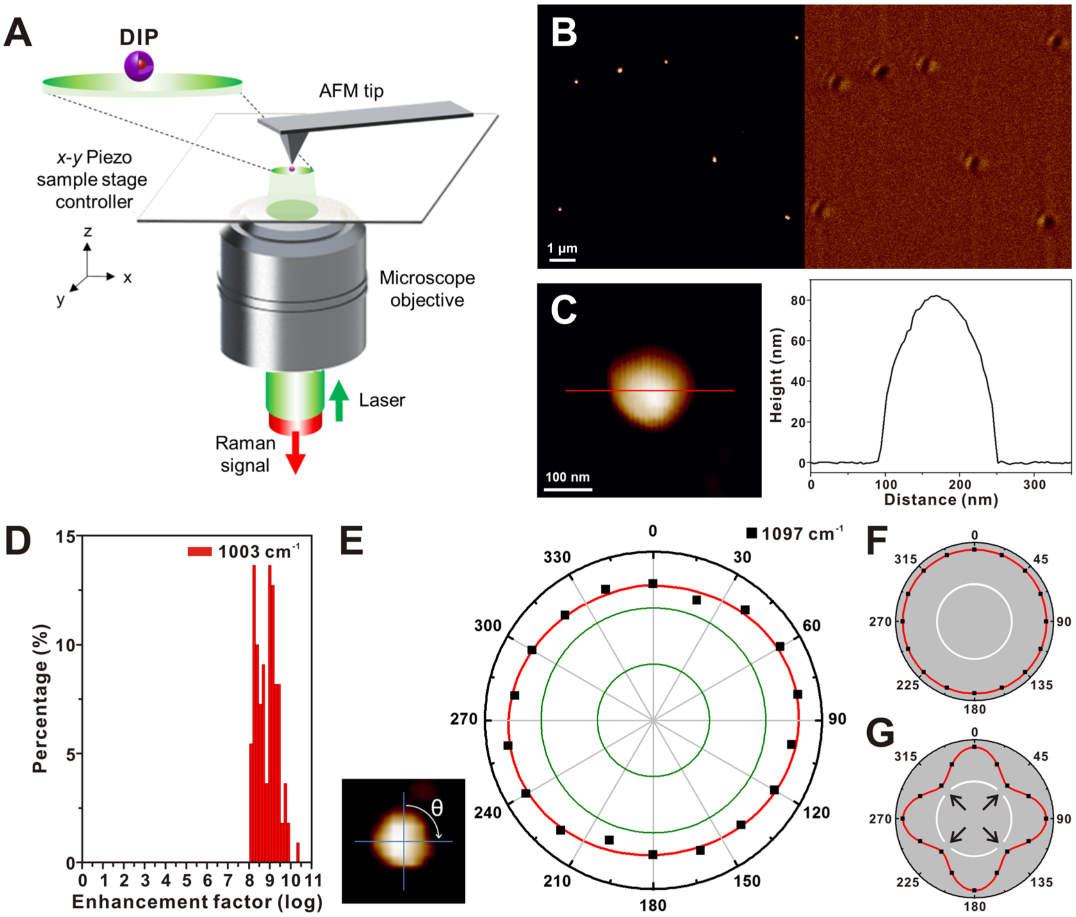

Figure 4. AFM-correlated Raman spectroscopy-based single-particle mapping analysis, SERS enhancement factor (EF) distribution, and polarization-resolved SERS plot for DIPs. (A) Instrumental setup used for AFM-correlated single-particle Raman spectroscopy. (B) Topographical matching of AFM image (left) and Rayleigh scattering image (right) for DIPs. (C) Magnified AFM image of a single DIP (left) and height profile across the NP (right, the red line in the AFM image). (D) A distribution of the SERS EF values at 1003 cm^{-1} as measured from individual DIPs (110 particles were analyzed). The EF values show a narrow distribution of large SERS EFs, range from 1.1 × 10^8 to 2.5 × 10^9 and 1.1 × 10^8 to 5.3 × 10^9 for 90.0% and 97.3% of particle populations, respectively. All the analyzed particles displayed the EFs of 1.1 × 10^8 or larger. (E) Single-particle polarization-resolved plot of the SERS intensity at 1097 cm^{-1} with respect to rotation angle (θ). (F and G) The calculated polarization-resolved plots of the EM field in the interior-nanogap region with respect to a rotation angle for (F) DIP and (G) Au-NNP, respectively. The theoretical calculations were performed using the finite element method with COMSOL, and the maximal values of the EM field enhancement at each rotation angle were plotted. The black arrows in panel G indicate Au nanobridges.

vivo and *in vitro* SERS imaging as well as photothermal therapeutic probes. On the other hand, the DIPs did not generate a detectable signal under excitation at a wavelength of 514 nm (Figure S7). Because the near-field enhancement of the SERS effect is determined by the plasmonic excitation mode near the resonance peak,[30] we believe that the 514 nm laser, whose wavelength is much different from that corresponding to the near-field resonance peak induced by the plasmonic excitation mode of the interior nanogap, could not generate a sufficiently strong EM field in the interior-nanogap region.

Single-Particle-Level SERS Analysis on DIPs. To investigate the optical properties of the DIPs in more detail, we performed an analysis of the SERS spectrum of the DIPs at the single-particle level using an atomic force microscopy (AFM)-correlated nano-Raman instrument (Figure 4A). To acquire the SERS spectra of the individual DIPs, we first accurately matched the end of the AFM tip with the focal spot of the objective lens (see details in Supporting Information). Then, we simultaneously obtained the AFM topographical image and the Rayleigh scattering image (Figure 4B) from the same particle. The representative tapping-mode AFM image (10 × 10 μm^2) indicated that the individual DIPs were well dispersed and did not overlap in the laser exposure focal spot (∼250 nm). Furthermore, high-magnification AFM images confirmed the spherical shape of the DIPs, with their height profile matching well with their overall size as determined from the TEM images (Figure 4C). We measured the SERS spectra of 110 individual DIPs and calculated the enhancement factor (EF) values for the fingerprint peak at 1003 cm^{-1} (see details in Supporting Information).

Figure 4D shows the distribution diagram of the EF values of the individual DIPs (110 particles were measured). The individual NPs exhibited detectable high-intensity SERS signals, and the EF values of the DIPs showed a narrow distribution, ranging from 1.1 × 10^8 to 2.5 × 10^9 for 90.0% of the population. Further, the distribution ranged from 1.1 × 10^8 to 5.3 × 10^9 for 97.3% of the population. Moreover, the EF values were as high as 2.1 × 10^{10} in some of the cases. Overall, all the particles generated the EFs of ≥1.1 × 10^8. It is worth noting that the narrow distribution of the EF values arises from the uniformly confined interior nanogap and the highly precise synthesis of the targeted structure in a high yield. Thus, such

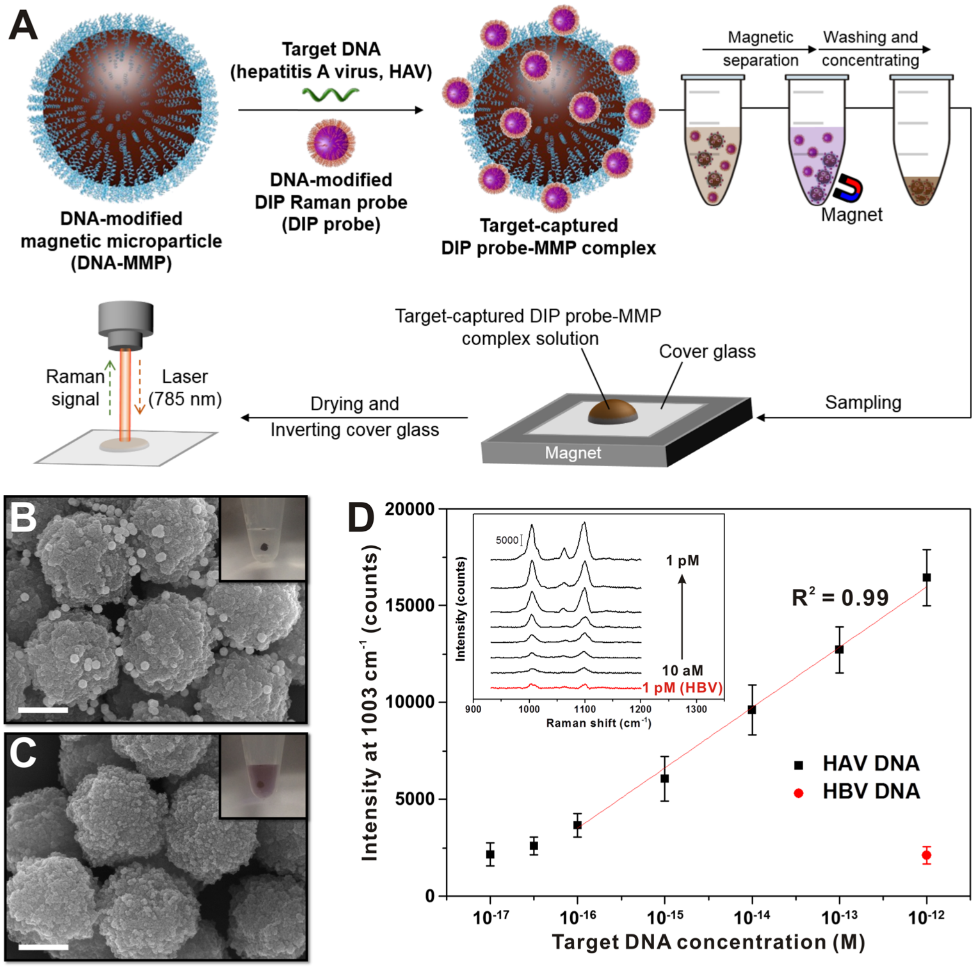

Figure 5. SERS-based ultrasensitive DNA detection assay using DNA-functionalized DIPs. (A) Schematic illustration of SERS-based ultrasensitive DNA detection assay with DNA-modified DIP nanoprobes that sandwich-capture target DNA with DNA-modified magnetic microparticles. (B and C) SEM images of target-DNA-specific sandwich hybridization complexes (target-captured DIP probe-MMP complexes) formed using different linker DNA [(B) complementary sequence DNA (HAV); (C) noncomplementary sequence DNA (HBV)]. Inset images: color of assay solution under external magnetic field after DNA sandwich hybridization. Scale bars are 500 nm. (D) SERS-based DNA detection assay results with DNA-modified DIPs (SERS intensities at 1003 cm^{-1} were measured for different DNA concentrations of HAV (10 aM to 1 pM) and HBV (1 pM). Inset: Change in SERS spectra obtained using different concentrations of target DNA. All the spectra were obtained using 785 nm excitation laser at laser power of 2 mW and acquisition time of 5 s. SERS intensities were obtained and averaged with consecutive accumulation of five measurements for each concentration.

structures with a nanogap can be exploited for use as reproducible and reliable SERS probes. It should be noted that the EF values of DIPs were conservatively underestimated by assuming the maximum number of 4-MPy molecules were uniformly packed on AuNP core surface (see details in Supporting Information). In addition, nonresonant Raman dyes (4-MPy) with a small cross-section were used in our study. The EF values of the DIPs are 2−3 orders of magnitude higher than those with other nanostructures reported previously for the same Raman dye molecule (4-MPy).[31−34] It is now widely accepted that an EF of 10^6 to 10^8 could be sufficient even for single-molecule detection.[16,21,35] In this respect, the as-synthesized DIPs, which generated very strong SERS signals with high sensitivity, are highly promising as SERS probes for use in various analytical applications. Significantly, we investigated the incident-laser-polarization-dependent SERS characteristics of the DIPs at the single-particle level (Figure 4E). In the case of anisotropic or assembled nanostructures, the optical properties are largely dependent on the geometric configuration and laser polarization direction.[36−38] In contrast, the DIPs exhibited stable and uniform SERS signals regardless of the polarization direction of the incident laser, owing to the symmetrically distributed hot spots within the interior nanogap. This polarization-independent property also makes the DIPs suitable for use as highly reliable, quantitative analytical probes. In the early stage of the synthesis of Au-NNPs with the nanobridges that connect an Au core and an Au shell, the extinction spectrum shows a new plasmonic resonance peak at ∼680 nm, which is caused by the anisotropically branched budding structures on DNA-modified Au cores.[21] On the other hand, a new extinction peak was not observed during the synthesis of the CAS NPs (Figure S3). These suggest that the proposed coreduction synthesis process results in the shell structures filled with a mixture of Au and Ag atoms, and relatively large clusters such as Au branched budding structures are not formed. This further suggests that, unlike Au-NNPs, the interior nanogap of DIPs consists of randomly distributed metal residues that can result in a symmetrically distributed EM field within the interior nanogap (Figure 4F,G).

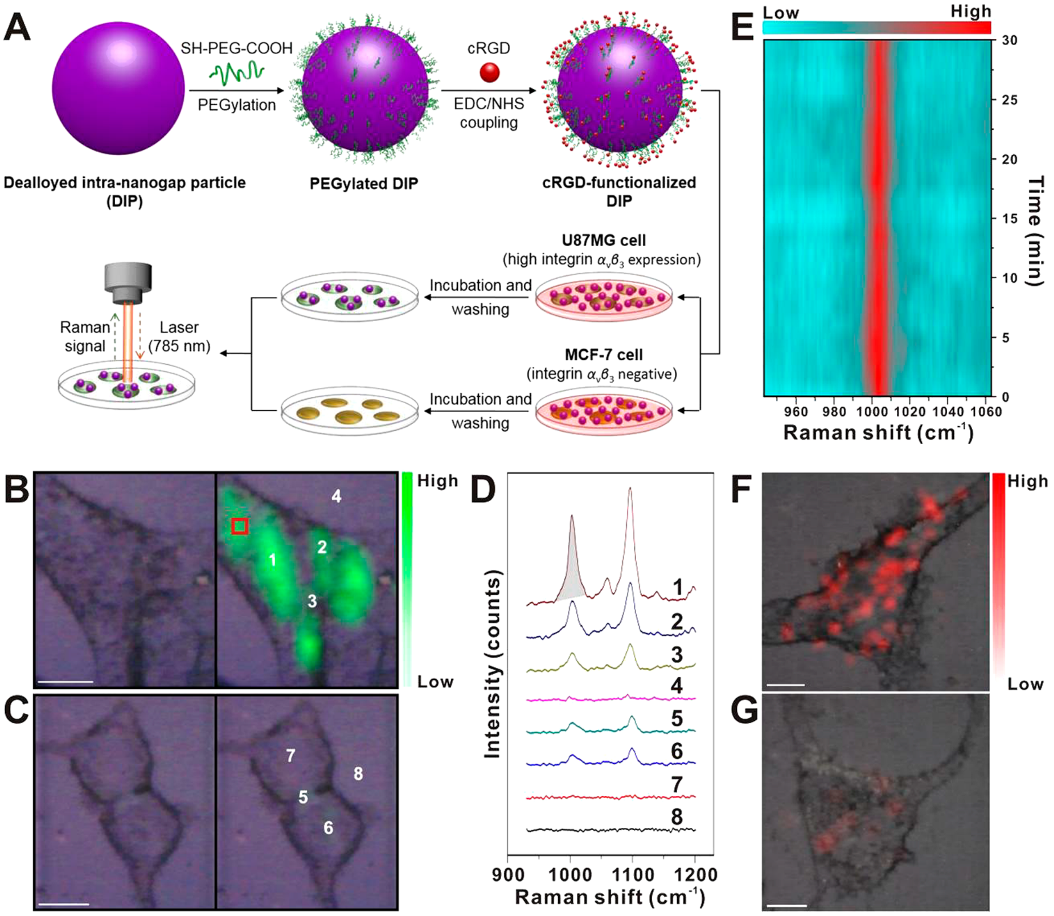

Figure 6. SERS-based integrin $\alpha_v\beta_3$-specific cell imaging using peptide-functionalized DIPs. (A) Schematic illustration of SERS-based target-specific cell imaging with cRGD-modified DIP nanoprobes. (B and C) Bright-field microscopy images (left) and SERS maps (right) of U87MG cells (B, high integrin $\alpha_v\beta_3$ expression) and MCF-7 cells (C, integrin $\alpha_v\beta_3$ negative) incubated with cRGD-functionalized DIPs. Scale bar is 10 μm. SERS intensity at each mapping pixel (2 μm × 2 μm) was integrated for SERS spectra ranging from 983 cm^{-1} to 1023 cm^{-1} indicated by the shaded region in Figure 6D and color-scaled for cell imaging. All the spectra were obtained using 785 nm excitation laser at 4 mW power and with acquisition time of 1 s. (D) The SERS spectra obtained from the numerically marked positions in Figure 6B and 6C. (E) Time-dependent Raman profiles of cRGD-functionalized DIPs in a cell measured within the red box in panel B. (F and G) SERS maps of U87MG cells incubated with cRGD-functionalized (F) DIPs and (G, average particle diameter of 80 nm) AuNPs, respectively. Scale bar is 10 μm. The SERS intensity at each mapping pixel (2 μm × 2 μm) was integrated for the SERS spectra ranging from 983 cm^{-1} to 1023 cm^{-1} and color-scaled for cell imaging. All the spectra were obtained using 633 nm excitation laser at 400 μW and with acquisition time of 1 s.

DNA Assays with DIPs. To test the potential of DIPs as SERS sensing bioprobes, we performed SERS-based ultrasensitive DNA detection assays using the NPs. In order to efficiently capture and separate target DNA, we used DNA-modified magnetic microparticles (DNA-MMPs) and DIP Raman probes (DIP probes) to detect the target DNA strands (hepatitis A virus DNA; HAV DNA), based on a typical sandwich-hybridization assay (Figure 5A, see details in Supporting Information). To confirm the formation of the sandwich hybridization complexes (target-captured DIP probe-MMP complexes) and its ability to undergo target-DNA-specific hybridization, we performed hybridization assays with complementary (HAV) and noncomplementary (HBV) DNA sequences (Figure 5B,C). In the presence of the complementary DNA, the solution turned colorless when an external magnetic field was applied to it, indicating the formation of the sandwich hybridization complexes (Figure 5B inset). In the presence of the noncomplementary DNA, however, the solution remained with the color even after the MMPs were collected with a magnet, meaning that the DIP probes were not captured by the DNA-MMPs (Figure 5C inset). Moreover, the formation of the sandwich hybridization complexes could be seen clearly in the scanning electron microscopy (SEM) images (Figure 5B,C). These results indicate that the proposed DNA detection method with DIPs is suitable for use in DNA detection assays. Figure 5D shows the changes in the SERS intensity at 1003 cm^{-1} for varying concentrations of target DNA (HAV) solutions (10 aM to 1 pM, black squares). The SERS intensity quantitatively decreases with a decrease in the concentration of the target DNA over a wide range. On the other hand, with the intensity of the SERS signal was very low during control experiments in which the target DNA was replaced with noncomplementary DNA (HBV) strands (1 pM, red circular dot). The limit of detection (LOD) was approximatively 10−100 aM, which is ~10 to 1000-fold higher sensitivity than the DNA detection results with other nanostructures and methods.[17,39−42] In terms of synthetic yield, structural precision, SERS EF distribution, and SERS signal stability and reproducibility, DIPs generated superior results over other SERS structures, resulting in highly sensitive and quantitative DNA detection. These results further confirm that the plasmonic DIPs fabricated with the SID process can be used as ultrasensitive DNA sensing probes in target-selective, ultrasensitive, and quantitative analytical SERS probes.

Targeted Cell Imaging with DIPs. Lastly, we performed SERS-based target-specific cell imaging using surface-functionalized DIPs (Figure 6A). To evaluate the integrin-targeting specificity of the DIPs, cyclo(Arg-Gly-Asp-D-Phe-Lys) (c-(RGDyK), hereafter denoted as cRGD) peptide, which specifically binds to integrin $\alpha_v\beta_3$ (overexpressed in metastatic and endothelial tumor cells), was attached onto the surfaces of the DIPs. Next, we introduced cRGD-functionalized DIPs into different cell lines, namely, U87MG (high integrin $\alpha_v\beta_3$ expression) and MCF-7 (integrin $\alpha_v\beta_3$ negative) (see details in Supporting Information). Owing to the high expression of integrin $\alpha_v\beta_3$ in the U87MG cells and its preferential binding affinity with respect to cRGD peptide, strong SERS signals were clearly observed in the integrin-$\alpha_v\beta_3$-positive U87MG cells, confirming the target-specific binding and SERS imaging capabilities of the cRGD-functionalized DIPs (Figure 6B,D). On the other hand, a SERS signal was barely detected in the case of the integrin-$\alpha_v\beta_3$-negative MCF-7 cells, confirming that the cRGD-functionalized DIPs showed good target selectivity for SERS-based cell imaging (Figure 6C,D). Importantly, the cRGD-functionalized DIPs generated uniform SERS signals steadily when they were continuously exposed by a laser for a long period (Figure 6E). DIPs produced more reliable, stronger SERS signals for cell imaging than AuNPs with a similar size (Figure 6F,G and Figure S8). It is worth noting that SERS-based cell imaging could be performed with a low-power laser (400 μW) and short exposure time (1 s for each pixel) with DIPs, which are critical in minimizing cell and tissue damage and stably imaging cells for a long-term.

CONCLUSIONS

We developed a selective, interdiffusive dealloying-based facile synthetic strategy for forming highly SERS-active Au−Ag NPs (DIPs) containing a uniformly confined interior nanogap in a high yield (~95%). This strategy is a very simple, cheap, and efficient one for fabricating interlayer-free interior nanogap particles without using modulating interlayer materials, such as DNA, polymer, or silica shell. It was confirmed that the interior nanogap, as small as ~2 nm, was formed by selective Ag-etching and interdiffusion of Ag atoms from the Au−Ag alloy shell (SID process). It should be noted that metal residues were randomly distributed inside the gap. The NPs with the interior nanogap showed a highly enhanced SERS signal as compared to those of the shell-less or nanogap-less NPs with a similar size, owing to the strong EM field generated in the interior nanogap by strong plasmonic coupling between the core and the shell. Furthermore, the DIPs emitted robust, stable, and quantitatively reproducible SERS signals and exhibited a highly enhanced and narrowly distributed EFs, ranging from 1.1×10^8 to 5.3×10^9 for 97.3% of the particle population. Significantly, all the analyzed particles displayed the EFs of $\geq 1.1 \times 10^8$. We developed an ultrasensitive DNA detection assay with DIPs for 10 aM to 1 pM target concentrations that were clearly discernible with the SERS signals from DNA-modified DIPs. It was also shown the cRGD-functionalized DIPs can efficiently target integrin-overexpressed cells and generate uniform SERS signals steadily when they were continuously exposed by a laser for a long period. DIPs facilitated SERS cell imaging with a low-power laser (400 μW) and short exposure time (1 s for each pixel), and these allow for minimizing cell and tissue damages and stably imaging cells for a long-term (>30 min). Our synthetic strategy with the SID process offers new revenues in forming plasmonic nanostructures with a nanogap or strong plasmonic coupling without a need for an interlayer between two nanostructures (e.g., core and shell). DIPs show potential as strong, controllable, and quantitative SERS probes with a narrow distribution of high EFs without the dependence of a laser polarization direction, and can address the long-standing issues in SERS signal reproducibility, reliability, and quantification capability. Finally, DNA detection and cell imaging results with biofunctionalized DIP probes validate and provide the opportunities in utilizing SERS probes in sensitive, selective biosensing, bioimaging, and theranostic applications with a high reliability.[1,6,21,43−45]

ASSOCIATED CONTENT

Supporting Information

The Supporting Information is available free of charge on the ACS Publications website at DOI: 10.1021/acscentsci.7b00584.

> Experimental details, supplementary figures and table on synthesis and characterization of nanoparticles, Raman measurement, theoretical calculations, DNA assay, and targeted cell imaging (PDF)

AUTHOR INFORMATION

Corresponding Author

*E-mail: jmnam@snu.ac.kr.

ORCID

Jwa-Min Nam: 0000-0002-7891-8482

Notes

The authors declare no competing financial interest.

ACKNOWLEDGMENTS

This research was supported by Basic Science Research Program through the National Research Foundation of Korea (NRF) funded by the Ministry of Science and ICT (NRF-2016R1A2A1A05005430) and BioNano Health-Guard Research Center funded by the Ministry of Science and ICT (MSIT) of Korea as Global Frontier Project (H-GUARD_2013M3A6B2078947). This work was also supported by the National Research Foundation of Korea (NRF) grant funded by the Korea government (MSIT) (NRF-2017R1A5A1015365).

REFERENCES

(1) Nam, J.-M.; Oh, J.-W.; Lee, H.; Suh, Y. D. Plasmonic nanogap-enhanced Raman scattering with nanoparticles. *Acc. Chem. Res.* **2016**, *49*, 2746−2755.

(2) Huang, Y.-F.; Zhang, M.; Zhao, L.-B.; Feng, J.-M.; Wu, D.-Y.; Ren, B.; Tian, Z.-Q. Activation of oxygen on gold and silver nanoparticles assisted by surface plasmon resonances. *Angew. Chem., Int. Ed.* **2014**, *53*, 2353−2357.

(3) Liu, N.; Tang, M. L.; Hentschel, M.; Giessen, H.; Alivisatos, A. P. Nanoantenna-enhanced gas sensing in a single tailored nanofocus. *Nat. Mater.* **2011**, *10*, 631−636.

(4) Bao, W.; Melli, M.; Caselli, N.; Riboli, F.; Wiersma, D. S.; Staffaroni, M.; Choo, H.; Ogletree, D. F.; Aloni, S.; Bokor, J.; Cabrini, S.; Intonti, F.; Salmeron, M. B.; Yablonovitch, E.; Schuck, P. J.; Weber-Bargioni, A. Mapping local charge recombination heterogeneity by multidimensional nanospectroscopic imaging. *Science* **2012**, *338*, 1317−1321.

(5) Le Ru, E. C.; Etchegoin, P. G. Single-molecule surface-enhanced Raman spectroscopy. *Annu. Rev. Phys. Chem.* **2012**, *63*, 65−87.

(6) Kumar, A.; Kim, S.; Nam, J.-M. Plasmonically engineered nanoprobes for biomedical applications. *J. Am. Chem. Soc.* **2016**, *138*, 14509−14525.

(7) Zhang, X.; Young, M. A.; Lyandres, O.; Van Duyne, R. P. Rapid detection of an anthrax biomarker by surface-enhanced Raman spectroscopy. *J. Am. Chem. Soc.* **2005**, *127*, 4484−4489.

(8) Kleinman, S. L.; Frontiera, R. R.; Henry, A.-I.; Dieringer, J. A.; Van Duyne, R. P. Creating, characterizing, and controlling chemistry with SERS hot spots. *Phys. Chem. Chem. Phys.* **2013**, *15*, 21−36.

(9) Talley, C. E.; Jackson, J. B.; Oubre, C.; Grady, N. K.; Hollars, C. W.; Lane, S. M.; Huser, T. R.; Nordlander, P.; Halas, N. J. Surface-enhanced Raman scattering from individual Au nanoparticles and nanoparticle dimer substrates. *Nano Lett.* **2005**, *5*, 1569−1574.

(10) Wei, H.; Xu, H. Hot spots in different metal nanostructures for plasmon-enhanced Raman spectroscopy. *Nanoscale* **2013**, *5*, 10794−10805.

(11) Scarabelli, L.; Coronado-Puchau, M.; Giner-Casares, J. J.; Langer, J.; Liz-Marzan, L. M. Monodisperse gold nanotriangles: size control, large-scale self-assembly, and performance in surface-enhanced Raman scattering. *ACS Nano* **2014**, *8*, 5833−5842.

(12) Liu, K.; Bai, Y.; Zhang, L.; Yang, Z.; Fan, Q.; Zheng, H.; Yin, Y.; Gao, C. Porous Au-Ag nanospheres with high-density and highly accessible hotspots for SERS analysis. *Nano Lett.* **2016**, *16*, 3675−3681.

(13) Lee, C.; Robertson, C. S.; Nguyen, A. H.; Kahraman, M.; Wachsmann-Hogiu, S. Thickness of a metallic film, in addition to its roughness, plays a significant role in SERS activity. *Sci. Rep.* **2015**, *5*, 11644.

(14) Yue, W.; Wang, Z.; Whittaker, J.; Lopez-royo, F.; Yang, Y.; Zayats, A. V. Amplification of surface-enhanced Raman scattering due to substrate-mediated localized surface plasmons in gold nanodimers. *J. Mater. Chem. C* **2017**, *5*, 4075−4084.

(15) Shanthil, M.; Thomas, R.; Swathi, R. S.; Thomas, K. G. Ag@SiO_2 core-shell nanostructures: distance-dependent plasmon coupling and SERS investigation. *J. Phys. Chem. Lett.* **2012**, *3*, 1459−1464.

(16) Lim, D.-K.; Jeon, K.-S.; Kim, H. M.; Nam, J.-M.; Suh, Y. D. Nanogap-engineerable Raman-active nanodumbbells for single-molecule detection. *Nat. Mater.* **2010**, *9*, 60−67.

(17) Zhao, B.; Shen, J.; Chen, S.; Wang, D.; Li, F.; Mathur, S.; Song, S.; Fan, C. Gold nanostructures encoded by non-fluorescent small molecules in polyA-mediated nanogaps as universal SERS nanotags for recognizing various bioactive molecules. *Chem. Sci.* **2014**, *5*, 4460−4466.

(18) Bardhan, R.; Mukherjee, S.; Mirin, N. A.; Levit, S. D.; Nordlander, P.; Halas, N. J. Nanosphere-in-a-nanoshell: a simple nanomatryushka. *J. Phys. Chem. C* **2010**, *114*, 7378−7383.

(19) Song, J.; Duan, B.; Wang, C.; Zhou, J.; Pu, L.; Fang, Z.; Wang, P.; Lim, T. T.; Duan, H. SERS-encoded nanogapped plasmonic nanoparticles: growth of metallic nanoshell by templating redox-active polymer brushes. *J. Am. Chem. Soc.* **2014**, *136*, 6838−6841.

(20) Lin, L.; Zapata, M.; Xiong, M.; Liu, Z.; Wang, S.; Xu, H.; Borisov, A. G.; Gu, H.; Nordlander, P.; Aizpurua, J.; Ye, J. Nanooptics of plasmonic nanomatryoshkas: shrinking the size of a core-shell junction to subnanometer. *Nano Lett.* **2015**, *15*, 6419−6428.

(21) Lim, D.-K.; Jeon, K.-S.; Hwang, J.-H.; Kim, H.; Kwon, S.; Suh, Y. D.; Nam, J.-M. Highly uniform and reproducible surface-enhanced Raman scattering from DNA-tailorable nanoparticles with 1-nm interior gap. *Nat. Nanotechnol.* **2011**, *6*, 452−460.

(22) Oh, J.-W.; Lim, D.-K.; Kim, G.-H.; Suh, Y. D.; Nam, J.-M. Thiolated DNA-based chemistry and control in the structure and optical properties of plasmonic nanoparticles with ultrasmall interior nanogap. *J. Am. Chem. Soc.* **2014**, *136*, 14052−14059.

(23) Sun, Y.; Mayers, B.; Xia, Y. Metal nanostructures with hollow interiors. *Adv. Mater.* **2003**, *15*, 641−646.

(24) Zhang, Z.; Zhao, B.; Hu, L. PVP protective mechanism of ultrafine silver powder synthesized by chemical reduction processes. *J. Solid State Chem.* **1996**, *121*, 105−110.

(25) Silvert, P.-Y.; Herrera-Urbina, R.; Tekaia-Elhsissen, K. Preparation of colloidal silver dispersions by the polyol process. *J. Mater. Chem.* **1997**, *7*, 293−299.

(26) Kim, M.; Ko, S. M.; Nam, J.-M. Dealloying-based facile synthesis and highly catalytic properties of Au core/porous shell nanoparticles. *Nanoscale* **2016**, *8*, 11707−11717.

(27) Gonzalez, E.; Arbiol, J.; Puntes, V. F. Carving at the nanoscale: sequential galvanic exchange and Kirkendall growth at room temperature. *Science* **2011**, *334*, 1377−1380.

(28) Bohren, C. F.; Huffman, D. R. *Absorption and Scattering of Light By Small Particles*; Wiley: New York, 1983.

(29) Smith, G. B. Dielectric constants for mixed media. *J. Phys. D: Appl. Phys.* **1977**, *10*, L39−L42.

(30) Lombardi, A.; Demetriadou, A.; Weller, L.; Andrae, P.; Benz, F.; Chikkaraddy, R.; Aizpurua, J.; Baumberg, J. J. Anomalous spectral shift of near- and far-field plasmonic resonances in nanogaps. *ACS Photonics* **2016**, *3*, 471−477.

(31) Orendorff, C. J.; Gearheart, L.; Jana, N. R.; Murphy, C. J. Aspect ratio dependence on surface enhanced Raman scattering using silver and gold nanorod substrates. *Phys. Chem. Chem. Phys.* **2006**, *8*, 165−170.

(32) Liu, H.; Zhang, X.; Zhai, T.; Sander, T.; Chen, L.; Klar, P. J. Centimeter-scale-homogeneous SERS substrates with seven-order global enhancement through thermally controlled plasmonic nanostructures. *Nanoscale* **2014**, *6*, 5099−5105.

(33) Rodrigues, D. C.; de Souza, M. L.; Souza, K. S.; dos Santos, D. P.; Andrade, G. F. S.; Temperini, M. L. A. Critical assessment of enhancement factor measurements in surface-enhanced Raman scattering on different substrates. *Phys. Chem. Chem. Phys.* **2015**, *17*, 21294−21301.

(34) Song, W.; Wang, Y.; Zhao, B. Surface-enhanced Raman scattering of 4-mercaptopyridine on the surface of TiO_2 nanofibers coated with Ag nanoparticles. *J. Phys. Chem. C* **2007**, *111*, 12786−12791.

(35) Park, W.-H.; Kim, Z. H. Charge transfer enhancement in the SERS of a single molecule. *Nano Lett.* **2010**, *10*, 4040−4048.

(36) Ming, T.; Zhao, L.; Yang, Z.; Chen, H.; Sun, L.; Wang, J.; Yan, C. Strong polarization dependence of plasmon-enhanced fluorescence on single gold nanorods. *Nano Lett.* **2009**, *9*, 3896−3903.

(37) Lee, H.; Kim, G.-H.; Lee, J.-H.; Kim, N. H.; Nam, J.-M.; Suh, Y. D. Quantitative plasmon mode and surface-enhanced Raman scattering analyses of strongly coupled plasmonic nanotrimers with diverse geometries. *Nano Lett.* **2015**, *15*, 4628−4636.

(38) Wei, H.; Hao, F.; Huang, Y.; Wang, W.; Nordlander, P.; Xu, H. Polarization dependence of surface-enhanced Raman scattering in gold nanoparticle-nanowire systems. *Nano Lett.* **2008**, *8*, 2497−2502.

(39) He, Y.; Su, S.; Xu, T.; Zhong, Y.; Zapien, J. A.; Li, J.; Fan, C.; Lee, S.-T. Silicon nanowires-based highly-efficient SERS-active platform for ultrasensitive DNA detection. *Nano Today* **2011**, *6*, 122−130.

(40) Wang, H.; Jiang, X.; Wang, X.; Wei, X.; Zhu, Y.; Sun, B.; Su, Y.; He, S.; He, Y. Hairpin DNA-assisted silicon/silver-based surface-enhanced Raman scattering sensing platform for ultrahighly sensitive and specific discrimination of deafness mutations in a real system. *Anal. Chem.* **2014**, *86*, 7368−7376.

(41) Ngo, H. T.; Gandra, N.; Fales, A. M.; Taylor, S. M.; Vo-Dinh, T. Sensitive DNA detection detection and SNP discrimination using ultrabright SERS nanorattles and magnetic beads for malaria diagnostics. *Biosens. Bioelectron.* **2016**, *81*, 8−14.

(42) Su, J.; Wang, D.; Nörbel, L.; Shen, J.; Zhao, Z.; Dou, Y.; Peng, T.; Shi, J.; Mathur, S.; Fan, C.; Song, S. Multicolor gold-silver nanomushrooms as ready-to-use SERS probes for ultrasensitive and multiplex DNA/miRNA detection. *Anal. Chem.* **2017**, *89*, 2531−2538.

(43) Han, S.; Samanta, A.; Xie, X.; Huang, L.; Peng, J.; Park, S. J.; Teh, D. T. B. L.; Choi, Y.; Chang, Y.-T.; All, A. H.; Yang, Y.; Xing, B.; Liu, X. Gold and hairpin DNA functionalization of upconversion nanocrystals for imaging and in vivo drug delivery. *Adv. Mater.* **2017**, *29*, 1700244.

(44) Chen, Y.; Xianyu, Y.; Jiang, X. Surface modification of gold nanoparticles with small molecules for biochemical analysis. *Acc. Chem. Res.* **2017**, *50*, 310−319.

(45) Liu, Y.; Balachandran, Y. L.; Li, D.; Shao, Y.; Jiang, X. Polyvinylpyrrolidone-poly(ethylene glycol) modified silver nanorods can be a safe, noncarrier adjuvant for HIV vaccine. *ACS Nano* **2016**, *10*, 3589−3596.